Internal structure of electron-beam filaments

V. Nardi, W. H. Bostick, J. Feugeas,* and W. Prior
Stevens Institute of Technology, Hoboken, New Jersey 07030
(Received 8 April 1980)

Electron beams of tW/cm^2 ($\sim$0.4 MeV) which are split into filaments are produced by an inductive generator which transfers field energy to beam particles in 1–10-ns pulses. Target-damage analysis reveals the composite internal structure of each filament as a sequence of concentric circles with a discontinuous pattern. The nonuniform distribution of collectively accelerated positive ions within a filament contributes to resolve the filament structure which propagates at a speed $\sim 3c/4$ and can cross unaffected a 10^3-G magnetic field.

Data on filamentation of electron beams have been provided so far by experimental[1,2] and theoretical[3] work and by numerical simulations[4] which have stimulated our interest in the internal structure of these filaments. To generate electron beams (EB) we use a plasma-focus discharge (PF)[5] with different gases (H_2, D_2, ^{4}He; 20-kV, 9-kJ capacitor bank). The transfer of the capacitor energy to magnetic energy of the PF pinch occurs in 2.2 μs and from the pinch to electron and ion beams by a sequence of pulses (1–10 pulses can be observed in a single discharge) over a time interval from $\lesssim$5 ns up to 200–400 ns (by Rogowski-coil signals[5] from the beam current and by the duration of the x-ray pulses from the beam source).[6] The EB pulses have the same multiplicity as the peaks in the $|dI/dt|$ signal from the PF-electrode current I.[5] PF electrodes, beam-drift chamber, dielectric pipe (P) $\sim$50-cm long to focus the EB, target, and Rogowski coils (RC) arrangement are reported in Fig. 1(a). Data on the highly collimated EB (and on the ion beam) along the electrode axis and the energy spectrum have been reported by previous papers.[5-7] We are concerned here only with the EB which is ejected at 180° (i.e., in the rear direction from the same discharge region—near the anode front end—and at the same time as the ion beam emission at 0°)[8] and with the ions which are collectively accelerated by EB in the same direction as EB.

The EB has a broad energy spectrum, carries $\cong$10% of the capacitor-bank energy, and the electrons have energies from $\gtrsim$40 keV to several MeV. This spectrum has some variations from shot to shot as well as permanent features, specifically a peak at about 300–400 keV in all well-formed discharges[5] (i.e., a D_2 discharge with a neutron yield per discharge $n \gtrsim 0.5\bar{n}$, where $\bar{n} \cong 2\times 10^8$ is the mean value of n over 10^2–10^3 shots in 6 Torr of D_2; for other gases a similar definition of well-formed discharge can be obtained in terms, e.g., of x-ray-energy-emission per shot). The EB propagates inside the hollow anode (the center electrode, a pipe 15-cm long) and then in the drift chamber (a pyrex pipe of 35-mm diameter) at the rear end of the anode. By beam-induced damage on targets we detect the filamentary structure of the EB, the energy $\epsilon \sim 10^{-5}$–10^{-1} J of each of the $\sim 10^3$ filaments which form a beam pulse, the internal structure of each filament (filament diameter $D \approx 1$–300 μm), and a nonfilamentary component of the same beam which is spatially uniform within a cross section of $\sim$5-mm diameter. Two hollow-anode configurations have been used: (i) fully open and (ii) partially closed anode [Fig. 1(a)]. For configuration (ii) an RC coil which is located downstream from the end of the focusing pipe P gives a typical value of the net EB current I_e which is smaller by a factor $\sim 10^{-1}$ than the typical value $I_e \sim 1$–10 kA for configuration (i) (the signal from a RC upstream from the end of the focusing pipe is always vanishingly small even when the target damage indicates a very intense beam). Target damage indicates that for (ii) with P the beam is formed only by filaments; when I_e is small, current neutralization is achieved in the self-pinched (filamentary) mode of propagation. Tests with different values of ϕ_2 indicate that the high-energy component (>300 keV) of EB is generated near the electrode axis within a cylindrical region of $\sim$3-mm diameter. The charge carried by this high-energy component was measured with the Faraday-cup method for a single pulse of the EB after a polystyrene (PST) target (375-μm thick) with the same result (4×10^{-4}–10^{-3} C) as in Ref. 5. By (i) each pulse of EB current I_e has rise time $\Delta t \cong 1$–10 ns to a peak value $I_{eM} \sim 2$–10 kA from RC signals; from this net value of I_{eM} we have $\nu/\gamma \lesssim 0.6$ where ν is the number of beam electrons per classical electron radius e^2/mc^2 of beam length, $\gamma = (1 - v^2/c^2)^{1/2}$; the EB propagation velocity is $v = 0.76c$ (c = light speed) and it is obtained from the signals of two coils RC_2 and RC_3 [Fig. 1(a)] encircling the drift chamber (distance between coils L = 150 or 300 cm).

Our measurements of the attenuation α of I_{eM}

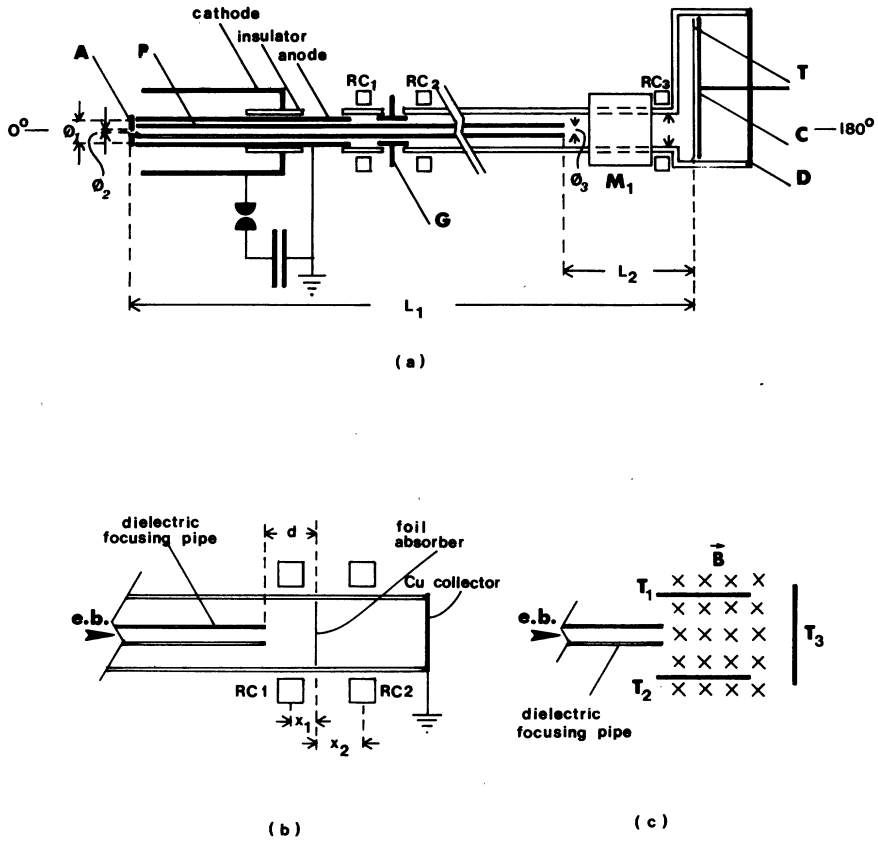

FIG. 1. (a) Schematic of PF and of EB drift chamber (filling gas and pressure, $p = 1$–25 Torr, is the same in discharge and drift chambers). A magnet (M_1) provides a 7 cm long B-field region. $L_2 \leq 1$–8 mm if $B = 0$. I_e signals for configuration (i) (fully open anode, $\phi_1 = 34$ mm) are 2–3 times higher than for configuration (ii) (partially-closed anode by disk A with central $\phi_2 = 4$-mm-diameter hole) without P. The support (C) of target (T) is either a floating plate or grid. (b) Setting to measure variations of return current by ion absorption ($0 \leq d \leq 22$ mm; $x_1 + x_2 = 3$ cm; $x_1 \geq 6$ mm). (c) Setting with magnetic field ($B \parallel$ to $T_{1,2,3}$ surfaces and $\perp$ to EB).

by (i)—$\alpha = [I_{eM}(RC_2) - I_{eM}(RC_3)]/I_{eM}(RC_2)$, where $I_{eM}(RC_{2,3})$ is the current from $RC_{2,3}$ signals—give $\alpha \cong 0.25$ on 150 cm and $\alpha \cong 0.5$ on 300 cm at $p = 6$ Torr of H_2 when the conducting ring G (at a distance 32 cm from the beam source) is not grounded [Fig. 1(a)]. An attenuation higher by a factor ~ 2 ($\alpha \cong 0.90$ over a distance of 300 cm) is instead observed if G is at ground potential. In this case the typical pulse current I_{eM} (2–10 kA) is, however, larger by a factor ~5 than in the case of a floating G. Higher values of I_{eM} and of α over a fixed traveling length L and a longer tail of each I_e pulse for a grounded G suggest that a floating G is charged by EB bombardment up to some negative voltage V_G; V_G then prevents electrons with a kinetic energy $< |eV_G|$ from propagating beyond G. Implications are (a) that these low-energy electrons contribute a substantial fraction of the beam net current and (b) that high-energy electrons (kinetic energy $> |eV_G|$) can propagate with small attenuation and with a substantial neutralization of current. The value of α increases with p and, for a grounded G, α is systematically higher in H_2 than in D_2 (by ~50% at 3 Torr, by $\lesssim$10% at 10 Torr; $L = 150$ cm). It is compatible with (a), (b), and $\alpha(H_2) > \alpha(D_2)$ to consider that the nonfilamentary component of EB can condense into filaments during the propagation of the beam in the drift chamber. By this process the high-current (nonfilamentary) component is depleted by increasing the current-neutralized (filamentary) component rather than by scattering in the background gas.

Filament condensation from a diffuse beam component, with a density increase by a factor 10^3–10^4, and a successive filament clustering are consistent with observed variations of damage depth and with the hierarchy of small-cavity clusters with diameter from $\cong 0.5$ μm up to $\cong 300$ μm on a target. We have used targets of plastic materials (a polymethylmethacrilate (PMMA) 5-mm-thick disk or a stack of one or more PST foils; each

foil is 125-μm thick), targets of a semiconductor material—label B—with a high value of the sublimation heat h_0 (~90 kcal/g atom) and different values of the distance L_1 ($6 \leq L_1 \leq 300$ cm) of the target from the beam source. Label B gives a maximum of space resolution (better than 0.5 μm) of the filament internal structure and is convenient for estimating ϵ; PST is more suitable for detecting charge effects and energy distribution of collectively accelerated ions inside a filament. The filament-induced damage is detected in the form of rings, bubbles, or holes on targets of plastic material (Fig. 2). Craters and surface exfoliation of circular regions instead of bubbles are detected in label B (Fig. 3). To estimate the filament energy ϵ we determine the mass M (g atom) of target material which is removed to form a filament-induced cavity and we take $\epsilon = Mh_0\xi$. ξ is a correction factor to account for the kinetic energy of the atoms ejected from the target; the value of ξ, $1 \leqq \xi \leqq 6$, depends on the model adopted for the blow-off process by which a crater is formed (in our case $\xi \cong 3$).

PST and label B targets complement each other well. The filament-induced rings in Figs. 2(a)–2(d) and correspondingly in Figs. 3(a)–3(c) and

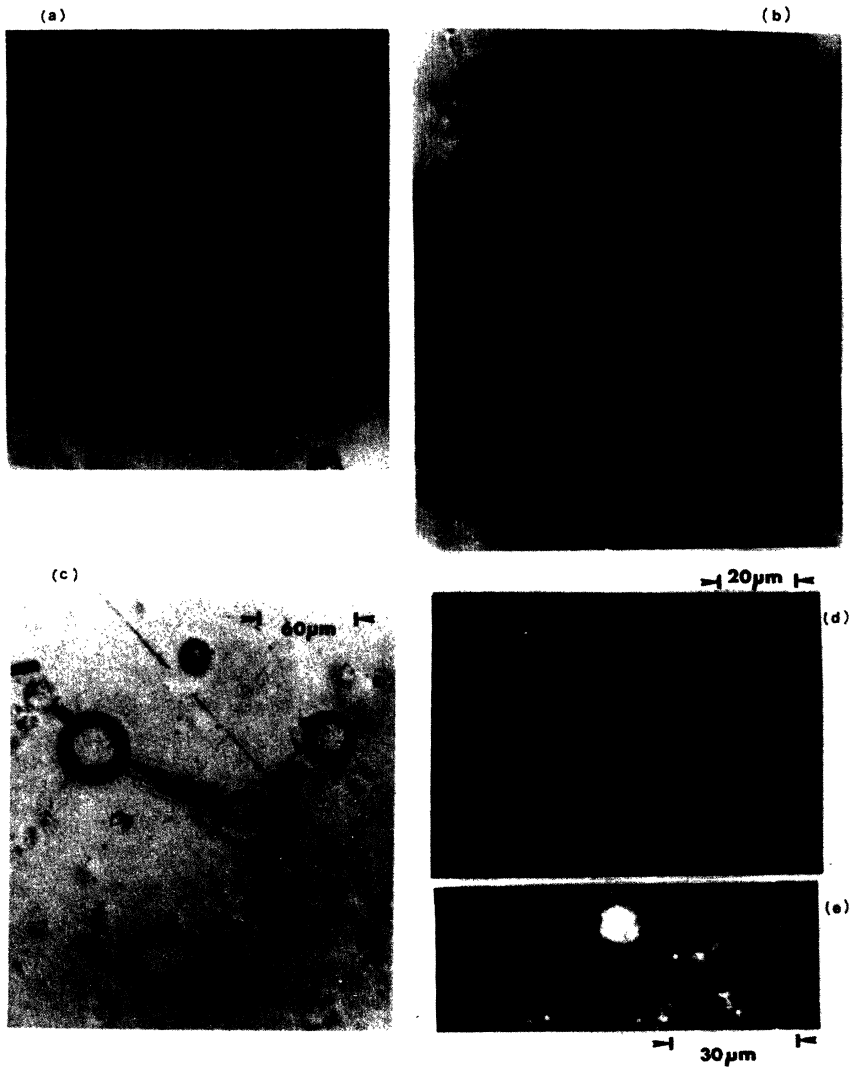

FIG. 2. Optical microscope photographs of filament markings on PST by (ii), $L_1 = 50$ cm, $L_2 = 3$ mm, exposure to a single discharge. (a) Note hole formed by pinched electrons at the center of large ($D \sim 4\tilde{D}$) ring with spokes under surface. (b) Same T showing discontinuous variation of ring width. (c) Surface-discharge pattern connecting rings. Outer circle is a cylindrical cavity ~30 μm below the target surface. (d) Deposited-ion bubble and ring with internal structure. (e) T surface is contaminated by positively charged (Cu, Zn oxides) dust $\gtrsim 1$ μs after exposure to EB. Dust-free (white) spots mark positive-charge deposition by EB (the dust is charged by photoionization before deposition on T).

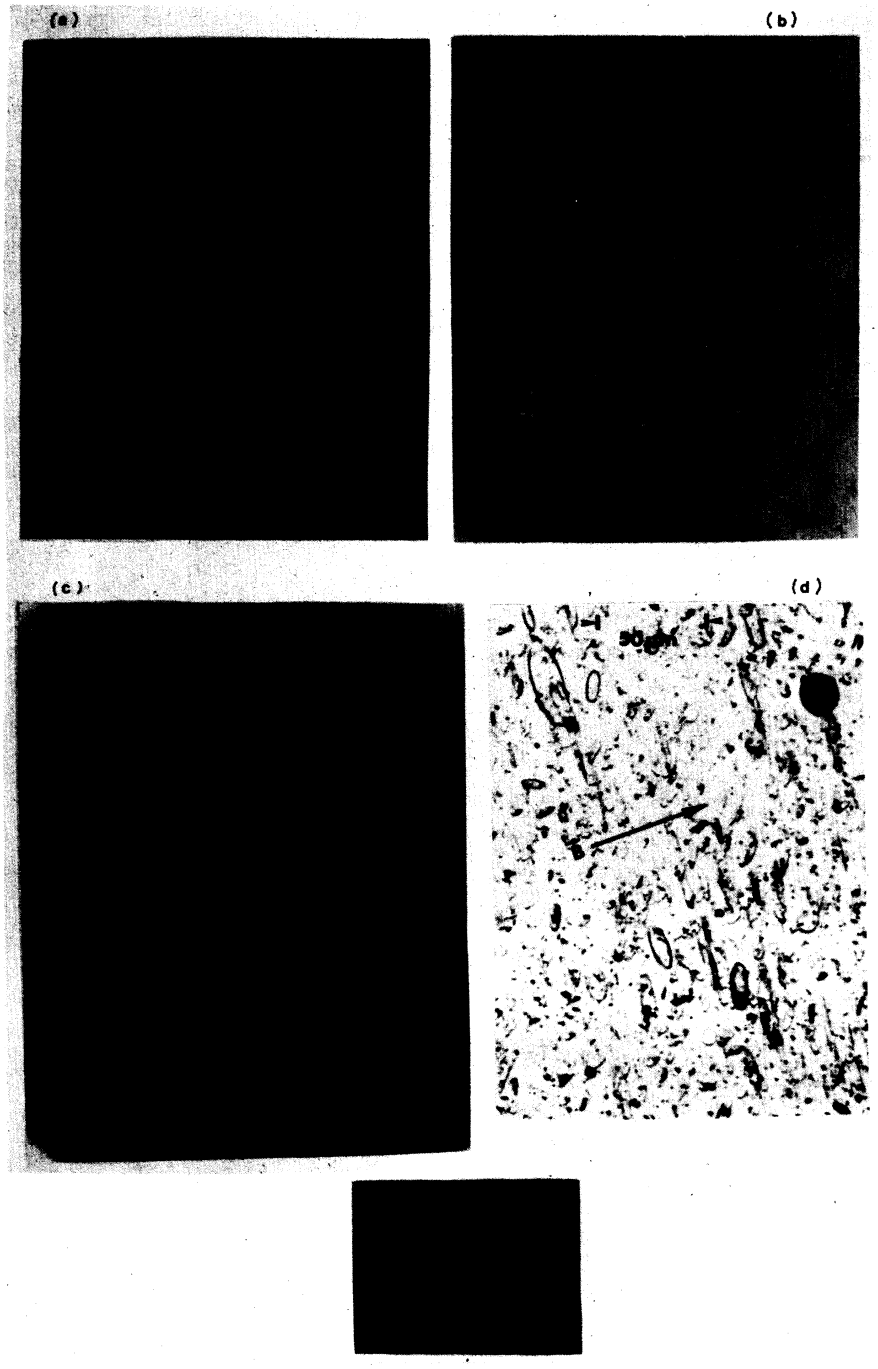

FIG. 3. Optical microscope photographs of filament markings on label B; $L_1 = 50$ cm, $L_2 = 8$ mm, and $B = 0$ for (a), (b), (c), and (e). (d) Damage on T_2, $B = 10^3$ G; note one deep circular marking and shallow elongated damage pattern. Circular markings only are observed also on T_1, T_3. (e) Layered filament components determining ring-width change in PST [Fig. 2(b)].

3(e) illustrate the different response of the two materials by irradiation under similar conditions (3 Torr, D_2 for Fig. 2, H_2 for Fig. 3). The non-filamentary component of the beam is detected by the formation of dendrites in a thick PMMA target which is ruptured through the irradiated volume (the dendrite-length distribution corresponds to the dominant value of the electron energy—~300–400 keV).[5] This beam component is depleted and the dominant value of the electron energy is

lowered for increasing values of L_1. Dendrites formation is not observed for $L_1 \gtrsim 50$ cm but distribution of the deposited charge and cross-section contour of the nonfilamentary component of the beam is still detectable on a PST target foil for $L_1 \gtrsim 300$ cm by the isochromatic pattern of the charge-induced stress in the foil.[9] We further consider only the filamentary component which tends to coalesce near the wall of the drift chamber [configuration (i)] for $L_1 \sim 300$ cm. This near-to-wall distribution of filaments is observed also by the x-ray image on conveniently screened x-ray films which have been used as targets in some discharge. A filament with a relatively high-energy density $4\epsilon/\pi D^2 \gtrsim 100$ J/cm^2 (by target damage) always penetrates the target surface by the orthogonal direction also if it approaches the target surface from an oblique direction. As an example, Figs. 3(a) and 3(c) report the damage on a orthogonal-to-P surface ($B=0$) at a distance $L_2 = 8$ mm from the end of P. The damage is located 10 mm outside the projection of the circular edge of P on the target surface so that the filament trajectory must have an inclination of at least ~45° in the gap between P end and target surface. The 90° penetration, as is recorded by the circular shape of the damage, and the nature of the filament-target interaction which produces it can be easily understood if the filament head has a high density of negative charge; in this case the approaching filament and the induced polarization current on the target form a current system with a minimum of magnetic energy when the filament is orthogonal to the surface.

The filament-induced damage indicates that the typical diameter $\tilde{D}$ of a filament for configuration (i) is usually smaller by a factor $\gtrsim 2$–3 than that for configuration (ii) with a focusing pipe P. We further report only data from this latter arrangement (P diameter $\phi_3 \sim 7.8$ mm) which give a more detailed picture of the filament internal structure (Figs. 2 and 3). Other important parameters which affect $\tilde{D}$ are m_i and $Z_i e$ ($m_i, Z_i e$ are the mass and charge of the fully ionized atom of the filling gas H_2 or D_2 or ^{4}He). The distribution within the interval $D = 1$–300 μm of the diameters of the filament-induced rings (as in Figs. 2 and 3) is peaked at $D = \tilde{D} \sim 30$ μm for H_2, ~15 μm for D_2, and ~10 μm for ^{4}He fillings. This dependence of D on eZ_i, m_i (and on the use of P) can be explained by considering that ions are accelerated by beam collective fields up to a maximum velocity $v_i < v$ (in the laboratory frame of reference) in the same direction as the electron-beam velocity v. For a given eZ_i ions with a smaller m_i^{-1} have a v_i smaller (and a $|v_i - v|$ larger) than that of ions with larger m_i^{-1} and they can more effectively achieve beam-charge neutralization than faster ions. By disregarding radial compression of ions, filaments can pinch to a smaller value of $\tilde{D}$ with a substantial increase of electron density for larger values of $|v_i - v|$ of the background ions. The observed dependence of D on the diameter of P implies that P can effectively increase the velocity of the accelerated ions. This is consistently verified by target damage. The circular cavity (~10–30-μm deep) at the border of a microscopic ring (Fig. 2), its depth λ under the target surface, and the internal structure of each ring can be observed by light reflection from the cavity wall through the transparent PST and by adjusting the microscope focal length on the chosen layer under the target surface. By a systematic inspection of more than 100 targets we conclude that each of these markings is produced by ion deposition when a beam filament crosses the target; the λ of a sharply defined cavity [Fig. 2(c)] indicates that ions with higher energy (1–2 MeV) are concentrated at the ring outer border and less energetic ions ($\lambda \sim 5$ μm) are inside the ring.[10] The filament electrons continue to propagate by further pinching after the ion deposition is completed and by forming a channel with diameter <1–5 μm which punches its way through the target (we follow with the microscope this filament pattern—from the bombarded surface to the rear surface of the target—for about 90% of all the circular markings that we have examined). The positive charge at a ring location reaches the peak value over the time interval $\Delta \sim l/0.76c \cong 1$ ns (l is the filament length); ns breakdown can then occur between the region below the PST target surface where the ions are trapped and the plasma outside the surface[11]; breakdown along the target surface can etch a positive Lichtenberg discharge pattern [Fig. 2(c)].[12] An alternative (internal) process of charge neutralization is depicted by the ring radial striations in Figs. 2(a) and 2(b) which form the discharge pattern ~10 μm under the target surface between the central region of the ring (positive voltage) and the outer ring border. We can control this charge neutralization process by replacing the target-supporting grid with a metal plate for collecting the electrons immediately behind the target. In this case surface-discharge patterns as in Figs. 2(a), 2(b), and 2(c) are not formed and ion-charge neutralization is achieved by a breakdown through the whole thickness of the target by a wiggling pattern which differs from the straight propagation channel of a pinched electron filament. Discharge patterns are not etched on a label B target; ϵ and the power-deposition ϵ/Δ are better assessed here than in PST targets (the depth ~10 μm of a crater as in the center of the

ring in Fig. 3(b) corresponds to $\epsilon/\Delta \sim 1$ tW/cm^2; crater diameter $\gtrsim 10$ μm when no ring pattern encircling the crater is formed). The dominant mode of beam propagation (filaments) at a distance $L_1 \lesssim 50$ cm from the source has been analyzed also by using a 10^3-G externally-applied magnetic field $\vec{B}$ [Fig. 1(c)]. The shallow ($\lesssim 1$-μm deep) elongated markings on target T_2 [Fig. 3(d)] are produced by filaments with $4\epsilon/\pi D^2 \ll 100$ J/cm^2 which are deflected by the magnetic field and hit obliquely the target surface. With $\vec{B}$ (orthogonal to P and parallel to T_1, T_2, and T_3 surfaces) this type of damage is observed only on T_2. Circular markings ($\lesssim 5$–10-μm deep) with a ringlike structure as in the upper right side of Fig. 3(d) are instead observed on T_1, T_2, and T_3 with or without $\vec{B}$. The absence of detectable effects of $\vec{B}$ on these penetrating filaments is consistent with filament current neutralization. Charge-induced repulsion among penetrating filaments and other EB components can dominate over the $\vec{B}$-field force and can cause the spread of the filaments in all directions at the end of P if a high value of net charge density coexists with current neutralization for each penetrating filament. Neutralization current by collectively accelerated ions within a filament is assessed by tests with two coils, RC 1, before a 50-μm-thick Mylar target, and RC 2, after the target [Fig. 1(b)]. The detected current by RC 2 is higher by a factor 4 ± 1 than the current by RC 1 (distance between RC 1 and RC 2 is ~3 cm; calibration and exchange of the coils by different shots have been performed). Return current can also be carried by counterstreaming electrons near the surface of each filament (low-energy electrons bake on the target surface a tenuous circular halo 2–10-μm wide which encircles a deep marking). We conclude that ion acceleration is most effective within a filament and can be enhanced by the filament-formation process. The concentration of positive ions in a filament is consistently indicated by observation of the following. (A) The discharge patterns which originate from a deep ring-shaped marking, typical of a positive Lichtemberg discharge [Fig. 2(c)] (the surface-discharge arms are longer and more detailed than by a relatively small and thick-limbed negative Lichtemberg discharge).[12] (B) The distribution of the dark contamination dust which leaves circular white patches where positive charge is concentrated [Fig. 2(e)]. (C) The increasing value of the EB net current I_{eM} after a $\gtrsim 50$-μm-thick Mylar target with the arrangement of Fig. 1(b). The formation of filamentary sheaths with sharp boundaries is possible by a variety of plasma conditions.[13] Further accretion of large filaments and of filament clusters by the capture of a filamentary-sheath fragment fits Fig. 3(e) and it seems a viable mechanism for the growth of composite filaments as it is the direct condensation from a diffuse beam. Our observations indicate that the self-pinched mode of propagation by filaments is not affected by hose and two-stream instabilities. Ion acceleration within the volume or at the surface of a filament can occur not only by electron beams from plasma focus discharges as (A), (B), and (C) indicate but also by other experiments in which more conventional types of relativistic-beam generators are used (the observation by ion-pinhole camera imaging of localized ion sources with linear dimension ~200 μm has been reported in the literature).[14] The observed β^+ decay of ^{13}N nuclei from $^{12}C(d,n)^{13}N$ reactions in our plastic targets is above noise level and we estimate that usually the accelerated deuterons with energy $\gtrsim 1$ MeV are less than 10^{10}. By increasing the generator energy and by a convenient focalization of filament clusters (rather than by focalization of single particle beams), beam-generating discharges can become a useful tool for pellet implosion in a fusion program[15] as it has been envisaged by other authors.[16]

This work was supported in part by the U. S. Air Force, Office of Scientific Research (Washington, D. C.) and the Office of Naval Research (Arlington).

---

*On leave from University of Rosario with CONICET support.

[1]C. A. Kapetanakos, Appl. Phys. Lett. 25, 481 (1974).

[2]J. Luce, W. H. Bostick, and V. Nardi, Lawrence Livermore Laboratory Report No. UCID-17232, 8/1976 (unpublished); in *Collective Methods of Acceleration*, edited by Rostoker and Reiser (Harwood, New York, 1979), p. 493.

[3]K. Molvig, G. Benford, and W. C. Condit, Phys. Fluids 20, 1125 (1977); E. S. Weibel, Phys. Rev. Lett. 2, 83 (1959).

[4]R. Lee and M. Lampe, Phys. Rev. Lett. 31, 1390 (1973).

[5]V. Nardi, W. H. Bostick, J. Feugeas, W. Prior, and C. Cortese, *Proceedings of the IAEA Conference on Plasma Physics and Controlled Nuclear Fusion Research*, Innsbruck, 1978 (IAEA, Vienna, 1979), Vol. 2, p. 143.

[6]W. H. Bostick, V. Nardi, and W. Prior, J. Plasma Phys. 8, 7 (1972); *Proceedings IAEA Conference*

(Berchtesgaden, 1976) (see Ref. 5), Vol. 3, p. 497.

[7]W. H. Bostick *et al.*, J. Nucl. Mater. 63, 356 (1976).

[8]By collimated measurements of D-D neutron and x-ray emission from the EB source (Refs. 6 and 7).

[9]D. Post, in *Measurement of Mechanical Properties, Part 2 (Techniques of Metal Research, Vol. 5)*, edited by R. F. Bunshah (Interscience, New York, 1971), Chap. 14.

[10]Filament-deposited net charge on PST foils is usually >0 [Fig. 2(c)] or ~0 [Fig. 2(a) and 2(b)]; charge >0 (low-energy ions) at center of filament marking whereas charge <0 may accumulate on outer border where low-energy electrons exceed by ~60% of the markings the high-energy ions per unit surface. This charge distribution is detected by target-contamination tests with positively charged dust; Fig. 2(e) shows the accumulation of the black dust at the border of dust-free (positively-charged) circular regions. Etching of ion tracks (with NaOH) on a CR-39-plastic target confirms that MeV ions are concentrated at the periphery of a filament.

[11]G. A. Vorobev and V. S. Korolev, Zh. Tekh. Fiz. 46, 2088 (1976) [Sov. Phys.—Tech. Phys. 21, 1222 (1976)]. PST targets evince a convenient polarity dependence of the ns breakdown voltage in a nonuniform (point electrode, or filament-induced) electric field.

[12]F. H. Merrill and A. von Hippel, J. Appl. Phys. 10, 873 (1939); G. C. Lichtenberg, Novi. Comment. Gött., 8, 168 (1777).

[13]J. S. DeGroot *et al.*, Phys. Rev. Lett. 38, 1283 (1977); see also V. Nardi, Phys. Rev. Lett. 25, 718 (1970).

[14]D. J. Johnson and J. R. Kerns, Appl. Phys. Lett. 25, 191 (1974).

[15]R. Martin (A.N.L.), in *Energy Storage, Compression and Switching II* (Plenum, New York, 1980).

[16]I. M. Vitkovitsky, L. S. Levine, D. Mosher, and S. J. Stephanakis, Appl. Phys. Lett. 23, 9 (1973).

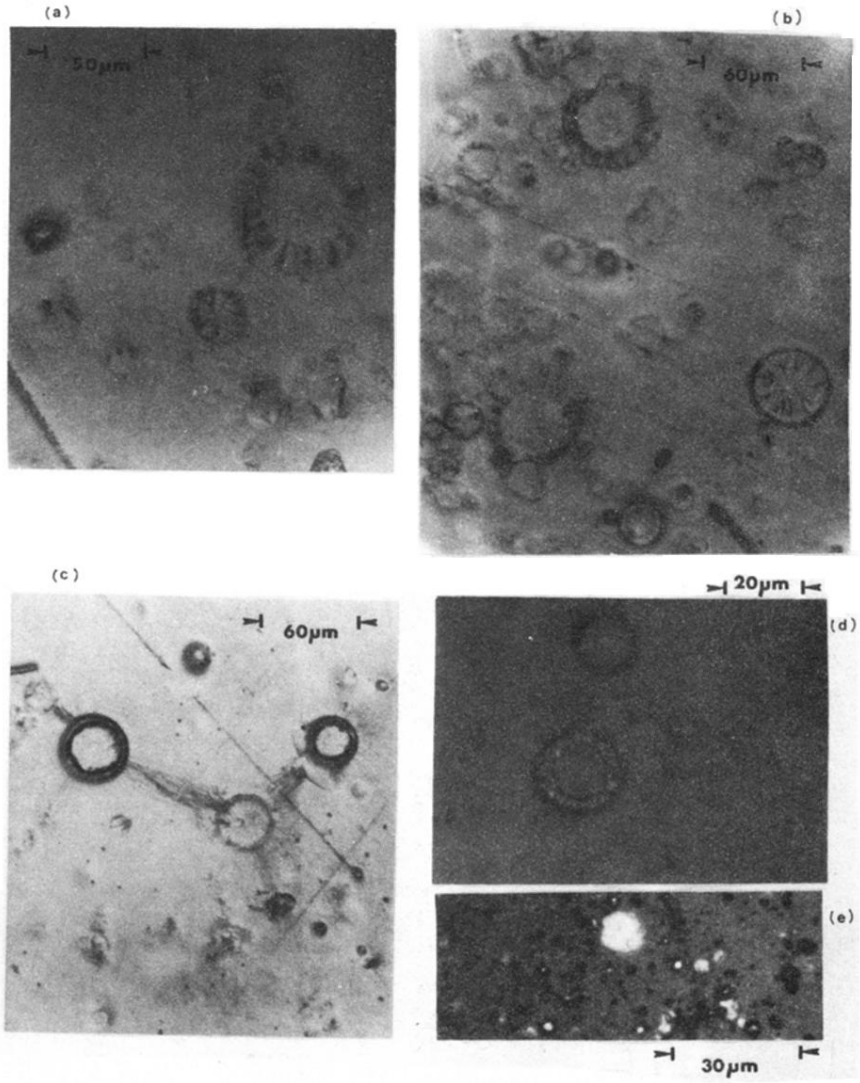

FIG. 2. Optical microscope photographs of filament markings on PST by (ii), $L_1 = 50$ cm, $L_2 = 3$ mm, exposure to a single discharge. (a) Note hole formed by pinched electrons at the center of large ($D \sim 4\tilde{D}$) ring with spokes under surface. (b) Same T showing discontinuous variation of ring width. (c) Surface-discharge pattern connecting rings. Outer circle is a cylindrical cavity ~30 μm below the target surface. (d) Deposited-ion bubble and ring with internal structure. (e) T surface is contaminated by positively charged (Cu, Zn oxides) dust $\gtrsim 1$ μs after exposure to EB. Dust-free (white) spots mark positive-charge deposition by EB (the dust is charged by photoionization before deposition on T).

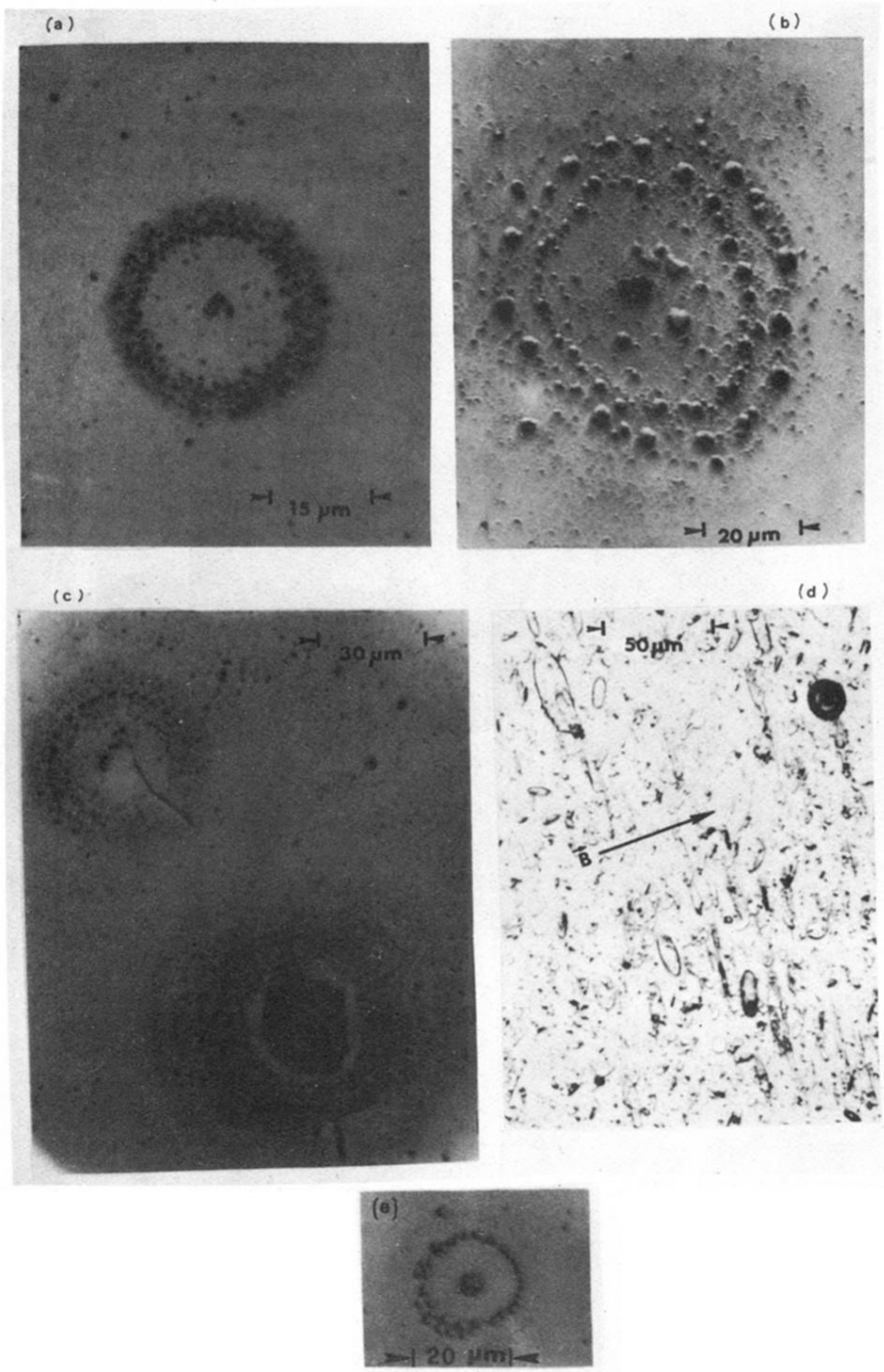

FIG. 3. Optical microscope photographs of filament markings on label B; $L_1 = 50$ cm, $L_2 = 8$ mm, and $B = 0$ for (a), (b), (c), and (e). (d) Damage on T_2, $B = 10^3$ G; note one deep circular marking and shallow elongated damage pattern. Circular markings only are observed also on T_1, T_3. (e) Layered filament components determining ring-width change in PST [Fig. 2(b)].